Direct Deposition of Copper Atoms onto Graphitic Step Edges Lowers Overpotential and Improves Selectivity of Electrocatalytic CO2 Reduction

Madasamy Thangamuthu (✉ madasamy.thangamuthu1@nottingham.ac.uk)

University of Nottingham   https://orcid.org/0000-0001-8391-3769

Tom Burwell

https://orcid.org/0009-0008-1003-6695

Gazi Aliev

Sadegh Ghaderzadeh

Emerson Kohlrausch

Yifan Chen

Wolfgang Theis

https://orcid.org/0000-0002-4074-8318

Luke Norman

Jesum Fernandes

Elena Besley

University of Nottingham   https://orcid.org/0000-0002-9910-7603

Pete Licence

Andrei Khlobystov

University of Nottingham   https://orcid.org/0000-0001-7738-4098

Article

Additional Declarations: There is NO Competing Interest.

Direct Deposition of Copper Atoms onto Graphitic Step Edges Lowers Overpotential and Improves Selectivity of Electrocatalytic CO₂ Reduction

Tom Burwell[1], Madasamy Thangamuthu[1*], Gazi N. Aliev[2], Sadegh Ghaderzadeh[1], Emerson C. Kohlrausch[1], Yifan Chen,[1] Wolfgang Theis,[2] Luke T. Norman[1], Jesum Alves Fernandes[1], Elena Besley[1], Pete Licence[3], Andrei N. Khlobystov[1*]

[1]School of Chemistry, University of Nottingham NG7 2RD, UK

[2]School of Physics & Astronomy, University of Birmingham B15 2TT, UK

[3]School of Chemistry, Carbon Neutral Laboratory, University of Nottingham NG7 2GA

Abstract

Minimizing our reliance on bulk precious metals is to increase the fraction of surface atoms and improve the metal-support interface. In this work, we employ a solvent/ligand/counterion-free method to deposit copper in the atomic form directly onto a nanotextured surface of graphitized carbon nanofibers (GNFs). Our results demonstrate that under these conditions, copper atoms coalesce into nanoparticles securely anchored to the graphitic step edges, limiting their growth to 2-5 nm. The resultant hybrid Cu/GNF material displays remarkable electrocatalytic properties in CO₂ reduction reaction (CO₂RR), exhibiting selectivity for formate production with a faradaic efficiency of ~94 % at a low overpotential of 0.17 V and an exceptionally high turnover frequency of 2.78×10^6 h⁻¹. The Cu nanoparticles adhered to the graphitic step edges significantly enhance electron transfer to CO₂, with the formation of $CO_2^{\cdot-}$ intermediate identified as the rate-determining step. Long-term CO₂RR tests coupled with atomic-scale elucidation of changes in Cu/GNF reveal nanoparticles coarsening, and a simultaneous increase in the fraction of single Cu atoms. These changes disfavour CO₂RR, as confirmed by density functional theory calculations, revealing that CO₂ cannot effectively compete with H₂O for adsorption on single Cu atoms on the graphitic surfaces.

Keywords: Electrocatalysis; Graphitic carbon nanofiber; Copper nanoparticles; Single-atom catalysts; CO₂ reduction.

Table of Contents Figure
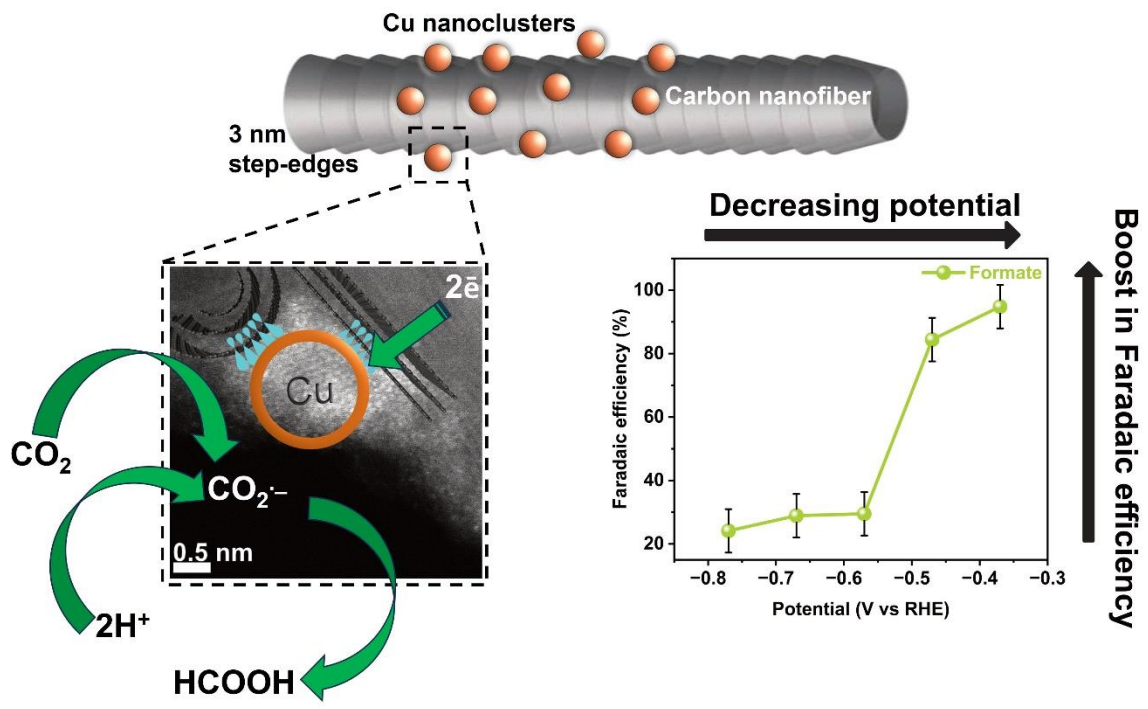
1. Introduction

The rising global population and industrialisation have increased our dependence on fossil fuels to meet our energy demands, resulting in the continuous emission of carbon dioxide (CO_2) into the atmosphere.[1] This ongoing trend necessitates the adoption of carbon capture and utilisation (CCU) as a critical component in future carbon-neutral or low-carbon economies to mitigate environmental damage.[2] A particularly promising approach involves converting captured CO_2 into sustainable fuels and high-value products, as it has the potential to address both the global energy demand and the management of CO_2 waste into industrially important chemicals to replace the use of petrochemicals. While various methods have been explored for CO_2 conversion,[3–7] electrocatalysis stands out as a primary choice as it offers the advantage of being compatible with renewable energy sources, allowing precise control over reaction rates and selectivity through applied voltage. Moreover, it is suitable for scaling up to industrial levels and operates efficiently under room temperature and atmospheric pressure conditions.[8,9]

Numerous studies have explored the electrochemical reduction of CO_2 into gas products *viz.* CO, CH_4 as well as liquid products *viz.* formate, methanol, and ethanol, using mostly noble metal-based electrocatalysts like Pt, Au, and Pd.[10–12] These electrocatalysts are extensively studied due to their exceptional activity; however, the low abundance of these metals and high cost constrain their practical applicability. As a promising alternative, more abundant transition metals such as Cu[13], Mn[14], Co,[15] Ni,[16,17] and Ag[18] have been demonstrated as effective electrocatalysts for electrochemical CO_2 reduction. Among these, Cu stands out due to its relatively high abundance, and ability to produce alcohols, C_2 and C_3 products.[19–21] More importantly, specific Cu surfaces exhibit a preference for adsorbing carbon monoxide (CO*) over hydrogen (H*) in aqueous electrolytes, a critical factor in preventing water reduction from competing with CO_2.[22,23] Furthermore, the CO binding energy of Cu (0.55 eV) is ideal for facilitating efficient CO adsorption and desorption, preventing electrocatalyst poisoning.[19,24] However, challenges persist when using Cu in the form of foils or large nanoparticles, as over 95% of the atoms are located below the surface and remain unutilised in the reaction.[25,26] This underscores the urgent need to advance the field of CO_2 reduction towards single metal atoms and sub-5 nm nanoparticles to maximise atom utilization efficiency and enhance selectivity control through the well-defined nature of catalytically active sites.

Recent advances have showcased the effectiveness of Cu single-atom catalysts (SACs) in the electrochemical reduction of CO_2 into CH_4.[27,28] For instance, Cu SACs loaded onto N-doped

3

porous carbon have been demonstrated to efficiently generate acetone with a faradic efficiency (FE) of 36.7%. This is attributed to Cu coordination with four pyrrole-N atoms, which creates crucial active sites, lowering the CO_2 activation energy and promoting C-C coupling.[29] Similarly, Cu SACs decorated within an N-doped carbon matrix, offering a CuN_4 coordination environment, facilitate ethanol production with a 55% FE at -1.2 V vs RHE.[30] Additionally, Cu SACs deposited on carbon nanofibers selectively produce methanol with a 44% FE, involving the formation of CO* intermediate followed by its reduction.[31] Despite these successes, the stability of SACs over prolonged reaction has been a concern due to the inevitable aggregation, resulting in selectivity loss and an increase in the onset potential for CO_2 reduction. To address this challenge, Cu nanoclusters (CuNCs), composed of a group of atoms, have emerged as materials that combine high stability with selectivity comparable to SACs.[32–34] For instance, electrochemical CO_2 reduction using CuNCs at -0.75 V vs RHE produces ethylene, ethanol, and n-propanol with a collective FE of 50% and consistent activity over a 10-hour reaction, highlighting the remarkable stability of nanoclusters.[35] Oxidised CuNCs, achieved through plasma treatment, exhibit improved stability and produce ethylene with a record FE of 60%.[36] Overall, Cu-based electrocatalysts have demonstrated significant promise in CO_2RR applications. However, precise control of the state and size distribution of active Cu centres greatly depends on the nature of the support material and the specific conditions of catalyst synthesis, which may involve wet impregnation, colloidal synthesis, or sublimation deposition methods traditionally used for the preparation of Cu nanoparticles, CuNCs or Cu SACs. In this context, engineering the metal-support interface at the atomic level and understanding its evolution during the reaction are essential to gaining precise control over CO_2RR electrocatalyst performance, and achieving an optimum balance of activity, selectivity, and stability.

In this study, we employ atomic deposition of Cu onto a nanotextured carbon surface to achieve a high-quality metal-carbon interface that allows investigation of electrocatalyst evolution at the atomic level, using advanced methods of electron microscopy and spectroscopy. Correlation of the structural data with the CO_2RR performance demonstrates that graphitic carbon step edges are of pivotal importance for the stabilisation of Cu in the form of small nanoparticles, which translates to high selectivity towards formate at low overpotentials. Augmented with computational modelling, analysis of structural changes in the Cu electrocatalyst taking place over time under CO_2RR conditions allows us to pinpoint the main

4

mechanisms responsible for the loss of selectivity, thus providing a strategy for the future design of highly efficient electrocatalysts for CO_2 reduction.

2. Results and discussion

2.1 Electrocatalyst Preparation and Characterisation

Magnetron sputtering was utilised for the deposition of Cu atoms directly onto GNFs (**Figure 1A**), which allows for a solvent-free synthesis of metal nanoparticles with no additional impurities, such as ligands, counterions yielding pure metal in direct contact with support material produced at high rate.[37] GNFs consist of stacked graphitic cones with approximately 3 nm step edges made up of rolled-up few layers of graphene, lining the GNF surface in a direction perpendicular to the main axis (**Figure 1B**). The highly textured surface of GNF presents an excellent opportunity for anchoring catalytic active centres onto the highly electrically conducting surface of GNF.[38]
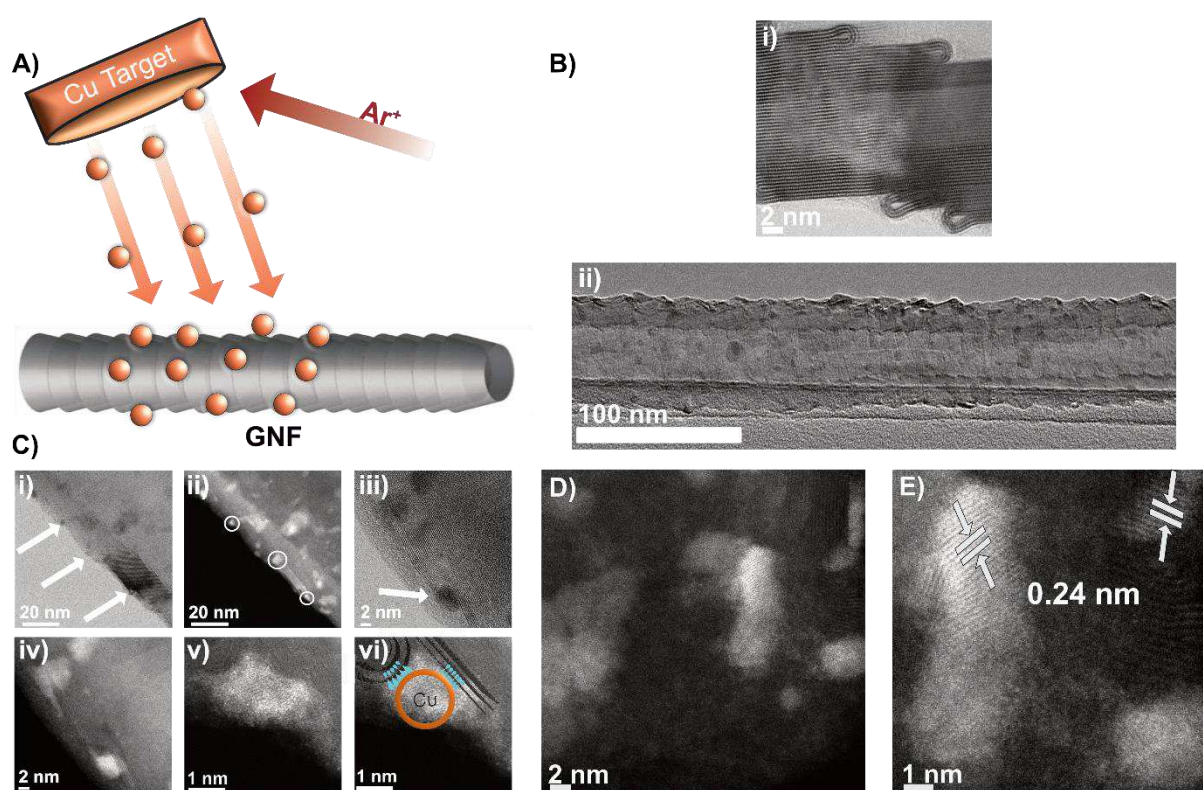
Figure 1. A) Schematic of magnetron sputtering delivering atoms of Cu directly onto the GNF surface, B)i) AC-TEM image of GNF step edges, and ii) TEM image of Cu/GNF C) TEM characterizations show Cu on the step pages: i) Bright-field image with arrows indicating Cu on step edges, ii) Dark field image with circles indicating Cu on step edges, iii) High magnification bright field image, iv) Dark field image, v) High magnification image illustrating Cu wedging itself into step edge and vi) with a very close metal-support contact, which indicates overlap of d-orbitals of the metal with π-system of the carbon lattice. D) Low magnification and E) magnified AC-STEM images indicating Cu species on the GNF.

This approach has been exploited for improving stability,[39] selectivity[40] or reusability of Pt, Pd, Rh, Cu, Au, Ru, Mo, and other metal catalysts in thermally or electrochemically activated reactions. Our recent investigations of atomistic mechanisms of this process revealed that at room temperature, metal atoms diffuse on the hexagonal lattice of support until they become immobilised at defect sites,[41] which in the case of GNF results in the nucleation of metal nanoclusters at the graphitic step edges (**Figure 1B**). Aberration-corrected scanning transmission electron microscopy (AC-STEM) imaging (**Figures 1C**, **D** and **E**) confirms that the majority of CuNPs are located on the step edges of the GNF (highlighted by arrows) typically reaching a diameter of 2-5 nm which appears to be dictated by the height of the step edges (**Figure 1C-iv**). Based on our microscopy observations, GNF step edges (**figure 1C-vi**) can provide the effective sites for Cu bonding directly to the carbon lattice, thus maximising electronic interactions between d-orbitals of the metal and π-electronic system of the graphitic layers, as evidenced by Cu "wedging" into crevices of the step edges (**figure 1C-v**), which could facilitate charge transfer between the metal and support as well as enhance the stability of the nanoparticles during reactions. Most nanoparticles are too small to form ordered crystal-like planes of atoms, however in some cases high magnification AC-STEM images reveal patches of ordered atoms with a lattice spacing of 0.24 nm which may correspond to (111) planes in $F_{m\text{-}3m}$ phase of CuO or $P_{n\text{-}3m}$ phase of Cu_2O (**Figure 1E**).

2.2 Electrochemical characterisation

The electrocatalytic activity of the Cu/GNF catalyst towards CO_2 reduction was studied using linear sweep voltammetry (LSV). The early onset potential of -0.3 V vs RHE at 0.1 mA/cm^2 current density in the presence of CO_2 compared to Ar (-0.5 V vs. RHE) (**Figure 2A-B)** demonstrates the activity of Cu/GNF towards CO_2 electrocatalytic reduction at a lower overpotential than previously reported for formate production (equation 1).

$$CO_2 + 2e^- + 2H^+ \rightarrow HCOOH \qquad -0.61\,V\,vs\,SHE \qquad (1)$$

The cathodic sweep also highlights the major reduction peak at +0.52 V corresponding to the reduction of Cu_2O to Cu, and a minor peak at +0.30 V corresponding to the reduction of CuO to Cu (**Figure S1**). Based on these results, we propose that when Cu/GNF is exposed to air, a fraction of the metal oxidises to Cu_2O on the surface of GNF, which is consistent with the XPS characterisation (see later). The charge transfer resistance of the Cu/GNF was studied using electrochemical impedance spectroscopy (EIS) in 0.1 M $KHCO_3$ electrolyte at a constant

potential of -0.78 V vs RHE within the frequency range from 10 kHz to 0.01 Hz and was used to obtain electrolyte resistance and the charge transfer resistance of the electrolyte-electrode interface.
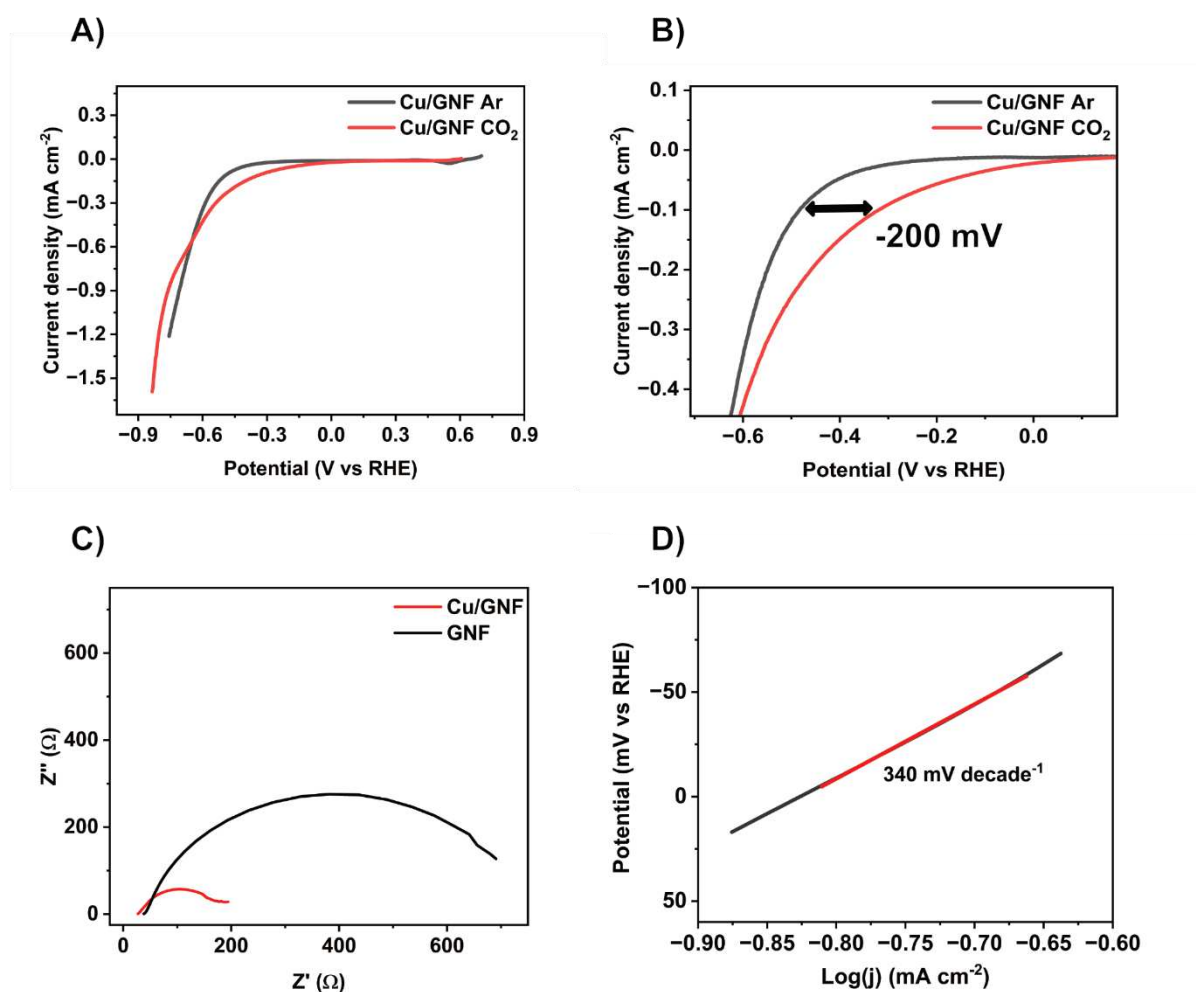
Figure 2. A) LSV of Cu/GNF measured in 0.1 M KHCO$_3$ sweeping the potential from 0.6 V to -0.9 V vs RHE with a scan rate of 10 mV s^{-1} B) onset potential shown for the CO$_2$RR of A, C) Nyquist plot of GNF with and without CuNPs obtained in 0.1 M KHCO$_3$ electrolyte at a constant potential of -0.78 V vs RHE within the frequency range from 10 kHz to 0.01 Hz and D) Tafel plot extracted from LSV.

The Nyquist plot of Cu/GNF shows a small semi-circle compared to the bare GNF suggesting that Cu loading significantly improved the charge transfer of the electrode (**Figure 2C**). The solution resistance R$_S$ is constant at 27 Ω for both electrodes, but the charge transfer resistance of the Cu/GNF is 154 Ω, significantly lower than the GNF without Cu (690 Ω) (**Figure 2C**), which indicates an intimate contact between highly conducting support (GNF) and catalytically active Cu centres in our electrocatalyst material.

LSV was used to further explore the CO$_2$ reduction reaction mechanism by extracting the current density and plotting the log of current density *vs* potential (**Figure 2D**). The slope of

7

the Tafel plot (**Figure 2D**) gives a gradient of 340 mV decade^{-1} suggesting that the formation of $CO_2^{\cdot-}$ intermediate is the rate-determining one-electron reduction step (equation 2), although such a high gradient suggests its sluggish kinetics.[42]

$$CO_2 + e^- \rightarrow CO_2^{\cdot-} \quad -1.9\,V \quad vs\,SHE \tag{2}$$

Overall, it can be concluded that the addition of Cu to GNFs greatly enhances charge transfer, while the surface of blank GNF has a large resistance and is not involved in catalysis. Therefore, Cu nanoparticles on GNFs significantly decrease charge transfer resistance thus improving the CO_2RR, while GNF provides a highly conducting support for Cu ensuring efficient delivery of electrons to the catalytic centres.

2.3 Selective CO$_2$ reduction into formate

The CO_2 reduction into liquid and gas products was studied using chronoamperometry at a desired constant potential in 0.1 M $KHCO_3$ in H-cell under continuous CO_2 saturation conditions; maintaining a constant CO_2 concentration in solution. ^1H NMR spectroscopy analysis of the reaction mixture after 2 h reaction reveals formate as the main liquid product formed by a proton-coupled reduction reaction (**equation 1**). In the range of potentials between -0.57 and -0.79 V, faradic efficiency for formate (FE$_{CHOO^-}$) is 20% and weakly dependent on the potential (**Figure 3A**). However, as the potential becomes less negative, FE$_{CHOO^-}$ increases sharply, reaching 94% for Cu/GNF with 0.84 wt% Cu metal loading; although there is a small minority of highly loaded GNFs, due to the shadow effect during sputtering, we focus on GNFs with representative loadings for electron imaging analysis. Surprisingly, Cu/GNF electrocatalyst with a higher content of Cu (3.38 wt%) is much less selective for formate formation, with FE$_{CHOO^-}$ reaching just 18%, especially at low overpotentials (**Figure S2**). From the data collected regarding higher Cu loadings on GNF, increasing mass loading of Cu increases nanoparticle size (**Figure S3A-C**), therefore changing the properties and selectivity of the Cu/GNF catalyst. It results in shifting selectivity away from formate as the major liquid product.[43]

To assess the impact of the Cu atomic deposition on GNF, we tested a similar Cu/GNF prepared by wet chemistry deposition of Cu on GNFs (**Table 1**). Under similar experimental conditions, wet chemistry Cu/GNF electrocatalysts exhibit FE$_{CHOO^-}$ of 43% and 20% at 0.31 and 1.32 wt% Cu loadings, respectively (**Figure S2**). Furthermore, we also tested the CO_2 reduction activity of Cu foil and observed FE$_{CHOO^-}$ of 40 % (**Figure S4**). Under CO_2 saturation at a potential of -0.38 vs RHE, faradic efficiency for H$_2$ evolution (FE$_{H2}$) represents 10% of the overall FE,

clearly demonstrating $\geq$ 90 % selectivity to CO$_2$RR products (**Figure 3A**), although with some FE attributed to H$_2$ due to the pH change incurred by CO$_2$ saturation. Moreover, in a potential range between -0.57 and -0.78 V, FE$_{H2}$ does exceed 10% FE, but with the lowest recorded value of 10% at -0.38 V (**Figure S5**), further corroborating the primary selectivity of Cu/GNF electrocatalysts for the CO$_2$RR at low potential(s).
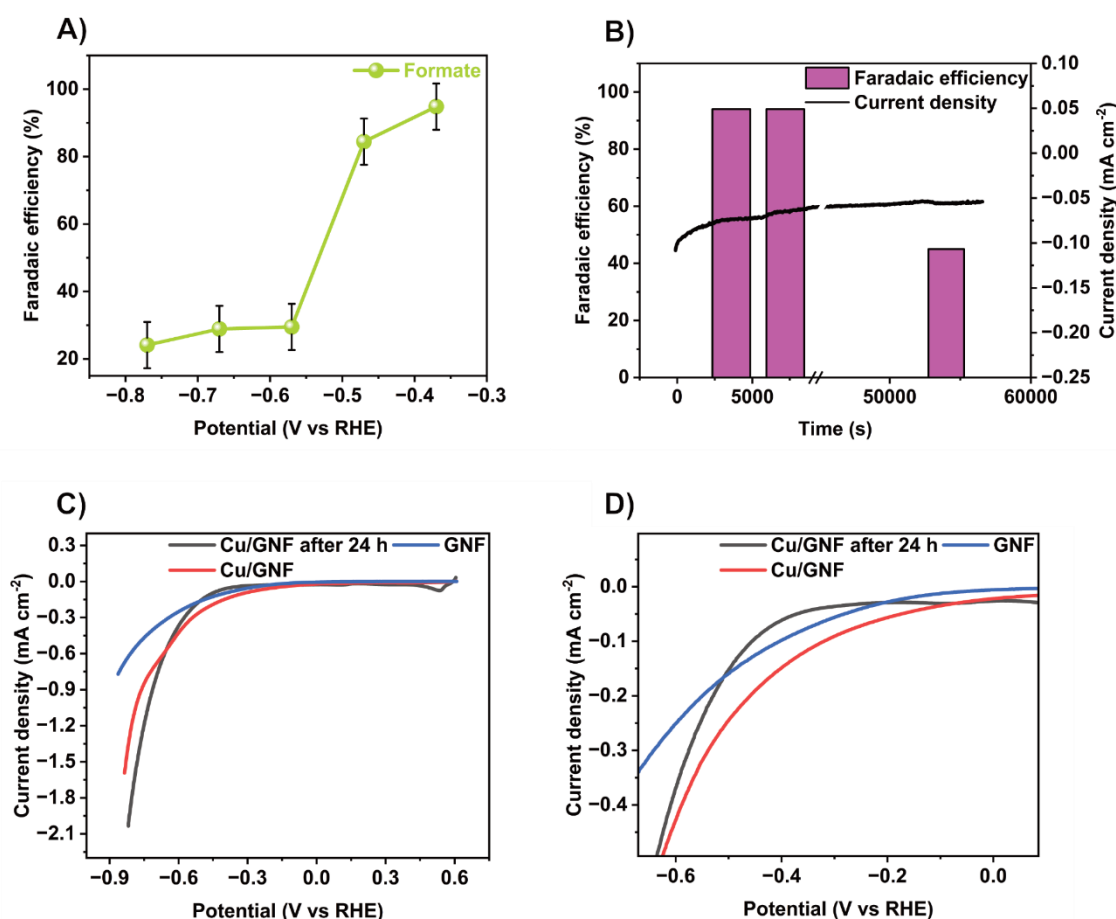
Figure 3. A) FE of formate from -0.78 V to -0.38 V, B) FE of formate over time with the current density of Cu/GNF (0.84 wt% Cu) at a constant bias of -0.38 V vs RHE, C) LSV from 0.6 to -0.9 V vs RHE ran at 10 mV s^{-1} in 0.1 M KHCO$_3$ fresh Cu/GNF vs used and blank GNFs and D) onset potential of the tested catalysts of D.

Overall, Cu/GNF demonstrated excellent selectivity for the formate, between -0.38 and -0.48 V vs RHE, also highlighted by the high TOF of 2.78×10^6 h^{-1} which is favoured at lower loadings of copper on GNFs. Compared to previously reported systems,[44–46] Cu/GNF has a significantly lower onset potential of CO$_2$ reduction to formate. Importantly, the loading method of metal on support plays a crucial role in the selectivity of the electrocatalyst, emphasising the significance of the quality of the metal-carbon interface for the CO$_2$R reaction.

Table 1. Comparison of faradaic efficiencies for CO_2 reduction to formate for different electrocatalysts studied in this work in 0.1 M $KHCO_3$ at room temperature.

| Catalyst	Preparation method	Cu loading (wt%)	Current density at -0.38 V vs RHE ($\mu A/cm^2$)	FE_{CHOOH} (%)	Partial current density ($\mu A/cm^2$)
Cu/GNF	Metal atomic deposition in vacuum	0.84	60	94	56.4
Cu/GNF	Metal atomic deposition in vacuum	3.38	200	18	36
Cu/GNF	Wet chemical deposition	0.31	70	40	28
Cu/GNF	Wet chemical deposition	1.32	90	60	54
Cu foil	N/A	N/A	47	40	18.8
GNF	N/A	N/A	3	<1	<<1

2.4. Stability of the electrocatalyst

To evaluate the stability of the electrocatalyst in selective formate production, an extended chronoamperometry run was performed on the most selective Cu/GNF (0.84 wt% Cu loading by atom sputtering) at a constant bias of -0.38 V vs. RHE. The current density j remains practically unchanged over 24 hours (**Figure 3B**) suggesting the electrocatalyst is very stable under the present working condition. The selectivity for formate remains above 90% for at least 2 hours, but then gradually starts decreasing as the reaction progresses further. Analysis of the reaction solution by inductively coupled plasma optical emission spectroscopy (ICP-OES) shows no detectable leaching of metal from Cu/GNF electrocatalysis. In a control experiment, where Cu nanoparticles are supported by GNFs without external step edges but instead, with a smooth graphitic surface, this catalyst was not investigated in detail due to low catalytic performance. It indicates that the active centres are not in a beneficial environment for CO_2 reduction compared to the GNF with external step edges (**Figure S6A-B**) and therefore show significantly less activity when compared to GNFs with step edges (**Table S1**) as well as flattening of the NP (**Figure S6B**) changing the surface morphology and demonstrating the importance of the nanotextured surface of support.

LSV analysis of Cu/GNF after 24 hours of the CO_2RR shows a small change in current density (0.2 mA cm^{-2} at -0.38 V vs RHE) compared to the initial catalyst, and a negative shift of the onset potential by -0.2 V (**Figure 3C-D**). The latter must be one of the primary reasons for the

drop in FE_{CHOO^-} after 24 hours, due to a change in the morphology of the catalyst and the emergence of single atoms (SAs) (**Figure 4F-H**). It is interesting that after 24 h of CO_2RR reaction, the properties of Cu/GNF prepared by atom sputtering become similar to those of Cu/GNF prepared by a wet chemistry method (**Figure S7**), which shows the onset potential of -0.6 V and FE_{CHOO^-} of 43 % right at the start of the reaction.

The CV of Cu/GNF after 24 h reaction shows two major reductive and oxidative peaks at the potentials 0.52 V and 0.34 V vs RHE owing to a mixture of both Cu(I) and Cu(II) but with a more prominent Cu(II) reduction peak not seen before catalysis, confirming morphological changes in the electrocatalyst (**Figure S8**).

AC-STEM imaging (**Figure 4A-D**) indicated several changes in the catalyst over time and it was observed after 2 hours that SAs were present, which was not seen in imaging before the reaction, this is thought to be due to peripheral Cu breaking from larger NPs, getting stuck in defect or detaching throughout the CO_2RR creating more SAs (**Figure 4E-H**). Continuing from this after 12 and 24 hours, an increase in NP size was observed, indicating Ostwald ripening, accompanied by the increase of SAs. This effect increases significantly from 2 to 12 hours and even more so for 24 hours. Image analysis at high magnification reveals a crystal lattice spacing of 0.18 nm which may correspond to (200) planes in the F_{m-3m} phase of metallic Cu, and 0.25 nm which may correspond to (111) planes in the F_{m-3m} phase of CuO or P_{n-3m} phase of Cu_2O (**Figure 4I-J**). The amorphous metallic copper was present before the reaction with localised domains which may be assigned to (111) planes of a copper oxide phase, but after the reaction, more SAs were present (**Figure 4F-H**). Although the current density does not change significantly over the 24-hour run, the FE for formate is decreased, which must be related to the changes in size and structure of Cu catalytic centres (**Figure S9**) (crystalline domains and SAs). The above fact can also be explained due to the change of Cu nanocrystalline domain and the possible phase restructuring during catalysis. For example, CO_2 reduction on Cu(111) surface is known to be selective for methane,[20,47] due to the short residence time of other reduction products, in particular CO. In the case of other Cu phases, the residency time of the products on the surface is longer leading to more substituted products.[43–45]

11
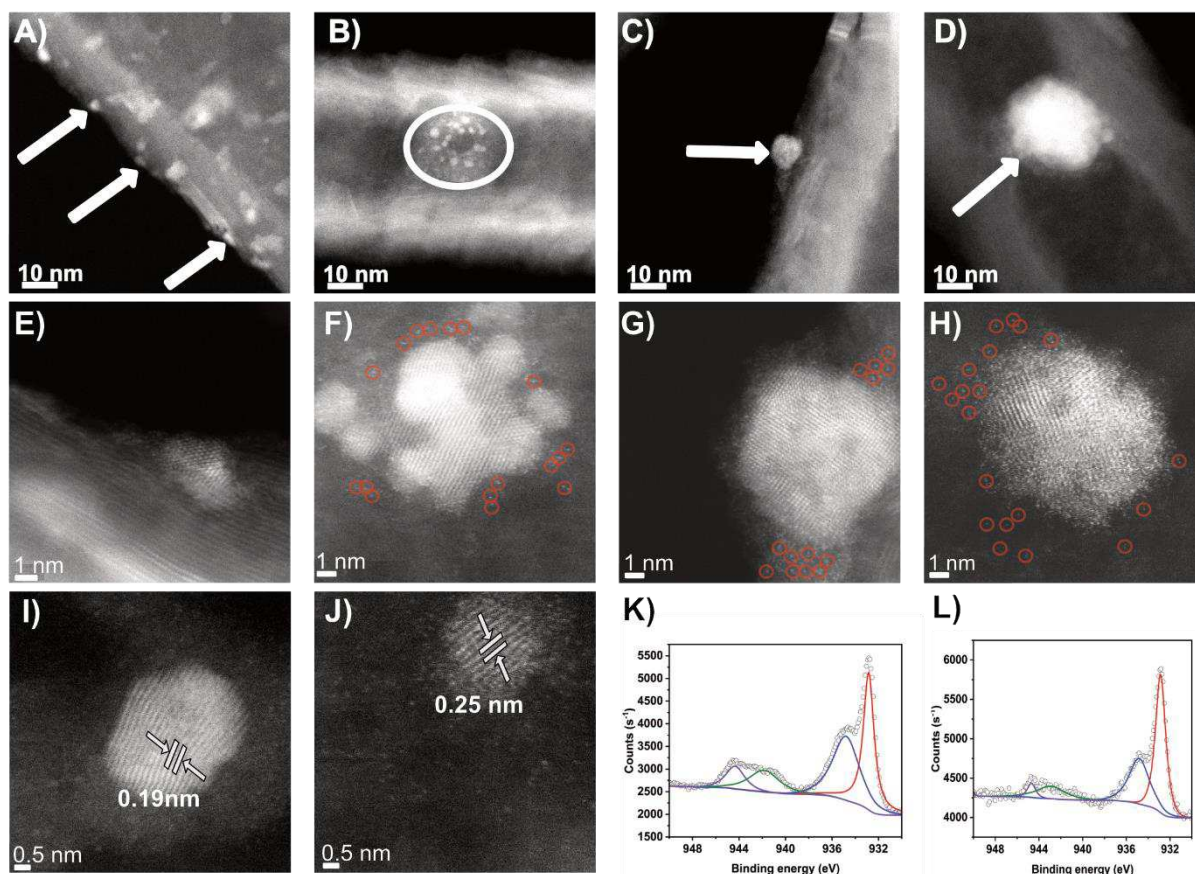
Figure 4. AC-STEM images of fresh and used Cu/GNF catalyst at -0.38 V vs RHE, A and E) fresh, B and F) 2 hours, C and G) 12 hours, and D and H) 24 hours. Fresh Cu/GNF on step-edge illustrating no SAs, where Cu/GNF after 2 hours with single atoms, and Cu/GNF after 12 hours showing more single atoms. I) Cu/GNF after 12 hours and J) Cu/GNF after 24 hours showing Cu crystal structure, H); XPS of fresh catalyst I) and after 24 hours J). XPS spectra of Cu/GNF K) before the reaction and L) after 24 h reaction.

We assessed the oxidation states of the Cu before and after electrocatalysis using X-ray photoelectron spectroscopy (XPS). The XPS spectra before the reaction (**Figure 4K**) show the deconvoluted core level peaks at 932, 934, 941 and 944 eV, corresponding to the Cu(I), Cu(II), Cu(II) satellite and the Cu(I) satellite, respectively.[48] XPS analysis of the electrocatalyst after 24 h reaction shows the same set of peaks (**Figure 4L**), but with the ratio of Cu(0) and Cu(I) increased (**Table S2**), suggesting that more metallic Cu is formed. However, we believe that in addition to the metallic copper, various oxidation states of Cu present which impact the catalytic activity for CO$_2$RR, agreeing well with previous reports.[49–51] It is worth noting that the distribution of oxidation states in Cu/GNF measured by XPS may not be representative under the present CO$_2$RR conditions, because the applied negative potential during the reaction favours metallic copper, therefore any post-reaction spectroscopy data must be treated with caution.

12

2.5 Density functional theory calculations of CO_2 and H_2O adsorption on copper

The selectivity of electrocatalytic reactions has been shown to be affected by the atomic surface structure of Cu face-centred lattice. For example, more stepped in nature lattice of Cu(311) surface is selective to CH_4, C_2H_4 and H_2, whereas the flat lattice surface of Cu(111) is more selective to methane.[52]
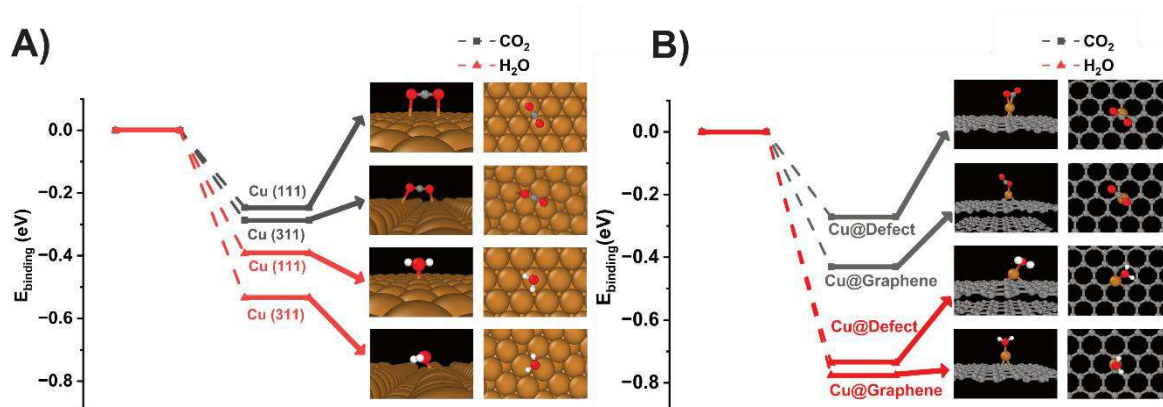
Figure 5. The binding energy of CO_2 and H_2O to A) bulk Cu(111) and Cu(311), B) Cu atom embedded in a vacancy defect in graphene and adsorbed on pristine graphene.

In order to understand the changes occurred during the catalysis, we compare Cu facets of Cu(111) and Cu(311) as a comparison crystal phase, measuring the binding energy of CO2 and the main competitor H2O. It is instructive to compare the binding energies on the Cu facets of Cu(111) and Cu(311) surfaces. Our density functional theory (DFT) results show that the binding of H_2O is stronger than CO_2 on both surfaces (**Figure 5A**), indicating that H_2O can effectively compete with CO_2 for the catalyst which may lead to an additional hydrogen evolution reaction on copper surfaces, as shown in earlier reports.[53,54] The difference in the binding energy of H_2O and CO_2 to the Cu(311) surface is 0.247 eV, which is higher than Cu(111), 0.147 eV, suggesting that water adsorption on Cu(311) is more favoured. As copper nanoparticles restructure during the reaction likely change the facets, the selectivity and faradic efficiency for CO_2 reduction products also change, as supported by earlier reports.[23,55]

The DFT calculations performed for a single Cu atom adsorbed on graphene and embedded in a vacancy defect indicate an even stronger bonding of H_2O, with the difference in the binding energy compared to CO_2 reaching 0.361 eV and 0.466 eV, respectively (**Figure 5B**). This indicates that CO_2RR can be disfavoured on Cu SAC as compared to nanoparticles, thus providing a possible explanation for the observed loss of FE_{CHOOH} and the shift in the onset potential for CO_2RR during our long-term electrocatalysis tests when single Cu atoms start emerging on GNF (**Figures 4F-H**).

13

Furthermore, our DFT results highlight favourable binding sites for CO_2 to Cu(111) and Cu(311) surfaces through the oxygen atoms (**Figure 5A**) leading to the preferential adsorption of CO_2, which agrees well with the earlier reports.[56,57] Kortlever *et al.*[57] suggested an initial electron transfer to the first intermediate $CO_2^{·-}$ followed by proton transfer, whilst Feaster *et al.*[58] proposed an initial concerted proton and electron transfer followed by desorption of formate. Nonetheless, formate being the major product in both cases confirms the effectiveness of Cu nanoparticles in the conversion of CO_2 to liquid products (**Figure S10**).

3. Conclusion

Copper-on-carbon systems have been recognised among some of the most effective electrocatalysts for CO_2 reduction, but many nanoscale mechanisms responsible for the activity, selectivity and stability of Cu remain unanswered. In this study, we have investigated the evolution of Cu on carbon surfaces and linked nanoscale structural changes with electrocatalyst selectivity for CO_2RR liquid products. The mode of nanoparticle formation from Cu atoms delivered directly onto the electrically conducting support, in the absence of any solvents or reagents, ensures a detailed investigation of the metal-carbon interface during the reaction. Carbon step edges of GNF support have been shown to play a role in the initial stabilisation of Cu nanoparticles which however evolve to a mixture of larger nanoparticles and single-atoms of Cu under CO_2RR conditions on the timescale of 2 - 24 hours. Metal atoms in the larger nanoparticles are more ordered than in the initial Cu nanoclusters and possess a surface that appears diminished CO_2 competition for active sites vs. H_2O (and the same applies to the single Cu atoms), as compared to initial smaller Cu nanoparticles. The structural changes lead to the decrease of selectivity for formate production due to the onset potential shifting to more negative values, but the overall activity of Cu/GNF remains high as Cu does not desorb from the highly textured GNF surface. Importantly, the present electrocatalyst Cu/GNF exhibits very high FE for formate at low potentials, but there is a need to improve efficiency and long-term stability. As this study identified Ostwald ripening and generation of SAs on carbon surfaces to be dominant processes affecting the performance of electrocatalysts, there is a need to suppress these by designing pertinent supports to effectively stabilise Cu nanoclusters or small nanoparticles through stronger bonding to the support. As the mode of metal deposition on GNF (atomic sputtering vs wet chemistry) and metal loading both are critically important for Cu/GNF selectivity, they must be considered alongside the nature of the support for future CO_2RR catalyst design.

4. Experimental section

4.1. Loading Cu onto GNF support

GNFs were supplied by PyroGraf (PR-24-XT-HHT) with iron content below 100 ppm. Before Cu sputtering, GNFs were heat treated in air (300 $^{\circ}$c) for 1 hour to remove superficial amorphous carbon on the surface. All depositions were carried out using an AJA magnetron sputtering system. Briefly, the GNF (0.35 g) were placed in the glove box and heated under vacuum for 5 hours (100 $^{\circ}$c) to remove any moisture. Then, the dried GNF were transferred to a custom-built stirring sample holder. The Cu deposition was carried out at room temperature with a working pressure of $3x10^{-3}$ torr using Ar gas and the Cu target (99.99%). The power applied to the system was 25 W for 30 minutes.

4.2. Preparation of wet chemistry Cu nanoparticles

To compare the CO2 reduction activity of sputter deposited Cu on GNF electrocatalysts, we prepared Cu nanoparticles using precipitation deposition method. In brief, 100 mg GNF was added into the 150 mL of DI water and stirred for 30 minutes at 80 $^{\circ}$c. Then, 0.1 mL (for 0.34 wt %) of 11 mg/mL copper nitrate solution was added into this mixture and stirred for a further 30 minutes. The urea was added into the above suspension at a ratio of 100:1 (urea to metal) and heated at reflux for 16 h. The resultant slurry was filtered under vacuum and washed with DI water (2 L) and dried for 10 h at 110 $^{\circ}$c. This dried catalyst is then reduced in 5% H_2/Ar for 1 hour at 230 $^{\circ}$c (5 $^{\circ}$c/min ramp rate) to remove the any organic residuals.

4.3. Characterisation

The Cu loaded on GNFs was quantified by ICP-OES using a Perkin-Elmer Optima 2000 spectrometer, with 10 mg of the catalyst digested in aqua regia (5 mL). The morphology of the sample was studied by scanning electron microscope (SEM) using JEOL 7000F Field Emission Gun microscope at 15 kV e-beam. The nanocluster size and atomic structure were characterized by a JEOL JEM-2100F aberration-corrected scanning transmission electron microscope equipped with a Cs probe corrector (CEOS) at a convergence angle of 20 mrad and annular dark field detector (ADF) operating with an inner angle of 36 mrad and outer angle of 82 mrad at 200 kV. The bright field (BF) detector was also used in parallel. The oxidation state of the Cu was characterised by an X-ray photoelectron spectroscope (XPS) using a Kratos Axis Ultra DLD instrument, fitted with an aluminium anode, and operated at 15 kV and 10 mA with a chamber pressure of $6.7x10^{-7}$ Pa. Wide energy range was acquired from 0 – 1400 eV with a step of 0.5 eV with a pass energy of 160 eV and a total scan time of 20 minutes. High-resolution scans used a step of 0.1 eV with a pass energy of 20 eV and a total scan time of 20 minutes. High-resolution data on the Cu 2p, O 1s and C 1s photoelectron peaks were collected. The X-

ray source was a monochromated Al Kα emission. The energy range for each pass was calibrated using Kratos Cu $2p^{3/2}$, Ag $3d^{5/2}$ and Au $4f^{7/2}$ three-point calibration. Calibration of transmission function was performed using a clean gold sample for all lens modes and transmission generator software Vision II. The data was processed using CASAXPS and charge correction in reference to C 1s at 284 eV.

4.4. Electrochemical characterisation

All electrochemical experiments were performed in a standard three-electrode configuration at room temperature using the Metrohm autolab PGSTAT204 with FRAM32M module. The Cu-GNF electrocatalyst thin film on carbon paper (PTFE treated (5 wt%) Toray Carbon paper-060) with a geometric surface of 1 x 1.5 cm^2 was used as the working electrode. Graphite rod and Ag/AgCl (3 M NaCl) were used as counter, and reference electrodes, respectively. The observed potentials against Ag/AgCl are iR corrected and converted into RHE using the Nernst equation: $E_{(RHE)} = E_{(Ag/AgCl)} + 0.21 + 0.0596 \times pH$. The catalyst ink was prepared by suspending the 10 mg of catalyst in 1 mL of ethanol or isopropanol and 80 µl of 5wt% Nafion® resin followed by ultrasonication for 15 minutes. Then, the catalyst thin film was obtained by drop casting the 50 µl of the ink on carbon paper and dried at room temperature.

4.5. Electrocatalysis

Electrocatalysis experiments were performed in a gas-tight two-compartment electrochemical cell (Ossila). The cathode and anode compartments were separated by Nafion®117 proton exchange membrane (Sigma Aldrich). Both compartments were filled with 30 mL of 0.1 M $KHCO_3$ solution (pH 8.34), (leaving 45 mL gas headspace) and pre-saturated with CO_2 for 30 min before the catalysis experiment. The carbon paper with an electrocatalyst layer and Ag/AgCl (NaCl 3 M) reference electrode was placed in the cathode compartment and the graphite rod was placed into the anode chamber. The CO_2 gas was continuously bubbled into the electrolyte during the reaction with a flow rate of 5 sccm. Chronoamperometry at a desired constant bias was performed with Metrohm autolab PGSTAT302N.

4.6. Product analysis

Gas products were measured by an Agilent 8890 gas chromatography instrument equipped with a flame ionisation detector (FID) and thermal conductivity detector (TCD). High-purity Ar was used as carrier gas. The FE of the gas products was calculated using equation (3).

$$FE(\%) = \frac{Q_{product}}{Q_{total}} \times 100 = \frac{n \times F \times f_{gas} \times t \times Product_{moles}}{Q_{total} \times 24.4x10^3} \times 100 (3)$$

Where n number of electrons to form one mole of product, F is the Faraday constant, f_{gas} is the flow rate of CO_2, t is time of injection, $product_{moles}$ is the number of moles of product, $24.4x10^3$ is the molar volume of 1 mole of gas and Q_{total} is the charge passed at time t. The peak area of the product was converted to the concentration using the calibration curve, which was obtained by a standard gas mixture.

The FE of the liquid products was calculated using equation 4.

$$FE(\%) = \frac{Q_{actual}}{Q_{total}} \times 100 = \frac{nZF}{Q_{total}} \times 100 \qquad (4)$$

Where Q_{actual} is the amount of charge needed to form n moles of product, Z is the electrons involved in the reaction and F is the Faraday constant. Q_{total} is the total amount of charge passed at the given time. The liquid products were measured by ^1H NMR spectroscopy using a Bruker AV(III) 500 with solvent (H_2O) suppression using equation (4). An aliquot of the electrolyte (400 μL) is added to D_2O (48 μL) and DMSO (40 μL, 4 mM) as an internal standard, and the concentration was calculated using equation (5).[58]

$$C_{product} = C_{standard} \times \frac{I_{product} \times H_{Standard}}{H_{product} \times I_{standard}} \qquad (5)$$

The $C_{standard}$, $I_{standard}$ and $H_{standard}$ are the concentration of the prepared standard (4 mM), the integrated area of internal standard and the number of hydrogens present on the standard, respectively. The $C_{product}$, $I_{product}$ and $H_{product}$ are the concentration of the product, the integrated area of the product peak, and the number of hydrogens present in the product molecule, respectively. Then, the FE of liquid products were calculated using equation (4). The turn-over frequency of the catalyst was calculated using equation (5) and further corrected by using equation (7 & 8).[59,60]

$$TOF = \frac{j_{tot} \times FE_{HCOO^-}}{2F \times n_{tot}} \qquad (6)$$

Where j_{tot}, n_{tot}, FE and F, represent total current density at steady state, the number of moles of copper atoms determined by ICP-OES, FE_{CHOO^-} is the FE of formate and F is the Faraday constant.

$$TOF_{corrected} = \frac{TOF}{f} \qquad (7)$$

Where f is equal to the ratio between surface-active Cu on the working electrode from the integrated charge of the anodic wave n (**Figure S11**) and the total moles determined *via* ICP-OES n_{tot} (equation 8).

$$f = \frac{n}{n_{tot}} \times 100 \qquad (8)$$

4.6. Density functional theory calculations

Spin-polarized Density Functional Theory (DFT) calculations were performed with the Vienna Ab initio Simulation Package (VASP)[61,62] using the projector augmented-wave (PAW) method and the Perdew–Burke–Ernzerhof (PBE) exchange-correlation functional.[63] The force tolerance of 0.03 eV Å^{-1} and 0.005 eV Å^{-1}, the electronic convergence of 10^{-5} eV and 10^{-6} eV and the energy cut-off of 660 eV and 450 eV were used for the Cu-surface and graphene, respectively. The Γ-point-centred Monkhorst−Pack k-point grid of $4 \times 4 \times 1$ was used to sample the Brillouin zone in both cases. Van der Waals interactions were considered using the DFT-D3 method,[64] with the Becke–Johnson damping function. The Cu(111) and Cu(311) periodic slab supercells consist of five and eight layers and contain 80 and 64 Cu atoms, respectively, and the graphene supercell contains 96 C atoms. The system size and calculation setup for the Cu(111) slab were adopted from a previous study.[65]

References

1. Gil-Alana, L. A. & Monge, M. Global CO2 emissions and global temperatures: Are they related. *International Journal of Climatology* **40**, 6603–6611 (2020).

2. Boot-Handford, M. E. *et al.* Carbon capture and storage update. *Energy Environ Sci* **7**, 130–189 (2014).

3. Wang, S. *et al.* CO2 Footprint of Thermal Versus Photothermal CO2 Catalysis. *Small* **17**, 2007025 (2021).

4. Sun, K., Qian, Y. & Jiang, H.-L. Metal-Organic Frameworks for Photocatalytic Water Splitting and CO2 Reduction. *Angewandte Chemie International Edition* **62**, e202217565 (2023).

5. Zhang, W., Ma, D., Pérez-Ramírez, J. & Chen, Z. Recent Progress in Materials Exploration for Thermocatalytic, Photocatalytic, and Integrated Photothermocatalytic CO2-to-Fuel Conversion. *Advanced Energy and Sustainability Research* **3**, 2100169 (2022).

6. Thangamuthu, M. *et al.* Polymer Photoelectrodes for Solar Fuel Production: Progress and Challenges. *Chem Rev* **122**, 11778–11829 (2022).

7. Li, C., Guo, R., Zhang, Z., Wu, T. & Pan, W. Converting CO2 into Value-Added Products by Cu2O-Based Catalysts: From Photocatalysis, Electrocatalysis to Photoelectrocatalysis. *Small* **19**, 2207875 (2023).

8. Wang, G. *et al.* Electrocatalysis for CO2 conversion: from fundamentals to value-added products. *Chem Soc Rev* **50**, 4993–5061 (2021).

9. Zhang, F., Zhang, H. & Liu, Z. Recent advances in electrochemical reduction of CO2. *Curr Opin Green Sustain Chem* **16**, 77–84 (2019).

10. Mustafa, A. *et al.* Progress and perspective of electrochemical CO2 reduction on Pd-based nanomaterials. *Chem Eng Sci* **245**, 116869 (2021).

11. Monteiro, M. C. O., Philips, M. F., Schouten, K. J. P. & Koper, M. T. M. Efficiency and selectivity of CO2 reduction to CO on gold gas diffusion electrodes in acidic media. *Nat Commun* **12**, 4943 (2021).

12. Umeda, M., Niitsuma, Y., Horikawa, T., Matsuda, S. & Osawa, M. Electrochemical Reduction of CO2 to Methane on Platinum Catalysts without Overpotentials: Strategies for Improving Conversion Efficiency. *ACS Appl Energy Mater* **3**, 1119–1127 (2020).

13. Nitopi, S. *et al.* Progress and Perspectives of Electrochemical CO2 Reduction on Copper in Aqueous Electrolyte. *Chem Rev* **119**, 7610–7672 (2019).

14. Siritanaratkul, B., Eagle, C. & Cowan, A. J. Manganese Carbonyl Complexes as Selective Electrocatalysts for CO2 Reduction in Water and Organic Solvents. *Acc Chem Res* **55**, 955–965 (2022).

15. Wu, Y., Jiang, Z., Lu, X., Liang, Y. & Wang, H. Domino electroreduction of CO2 to methanol on a molecular catalyst. *Nature* **575**, 639–642 (2019).

16. Yang, H. *et al.* Carbon dioxide electroreduction on single-atom nickel decorated carbon membranes with industry compatible current densities. *Nat Commun* **11**, 593 (2020).

17. Su, P., Iwase, K., Nakanishi, S., Hashimoto, K. & Kamiya, K. Nickel-Nitrogen-Modified Graphene: An Efficient Electrocatalyst for the Reduction of Carbon Dioxide to Carbon Monoxide. *Small* **12**, 6083–6089 (2016).

18. Liu, S., Sun, C., Xiao, J. & Luo, J.-L. Unraveling Structure Sensitivity in CO2 Electroreduction to Near-Unity CO on Silver Nanocubes. *ACS Catal* **10**, 3158–3163 (2020).

19. Kuhl, K. P. *et al.* Electrocatalytic Conversion of Carbon Dioxide to Methane and Methanol on Transition Metal Surfaces. *J Am Chem Soc* **136**, 14107–14113 (2014).

20. Nitopi, S. *et al.* Progress and Perspectives of Electrochemical CO2 Reduction on Copper in Aqueous Electrolyte. *Chem Rev* **119**, 7610–7672 (2019).

21. Yang, H. *et al.* Scalable Production of Efficient Single-Atom Copper Decorated Carbon Membranes for CO2 Electroreduction to Methanol. *J Am Chem Soc* **141**, 12717–12723 (2019).

22.Bagger, A., Ju, W., Varela, A. S., Strasser, P. & Rossmeisl, J. Electrochemical CO2 Reduction: A Classification Problem. *ChemPhysChem* **18**, 3266–3273 (2017).

23. Bagger, A., Ju, W., Varela, A. S., Strasser, P. & Rossmeisl, J. Electrochemical CO2 Reduction: Classifying Cu Facets. *ACS Catal* **9**, 7894–7899 (2019).

24. Ni, B. & Wang, X. Face the Edges: Catalytic Active Sites of Nanomaterials. *Advanced Science* **2**, 1500085 (2015).

25. Asperti, S., Hendrikx, R., Gonzalez-Garcia, Y. & Kortlever, R. Benchmarking the Electrochemical CO2 Reduction on Polycrystalline Copper Foils: The Importance of Microstructure Versus Applied Potential. *ChemCatChem* **14**, e202200540 (2022).

26. Darayen, J. *et al.* Porous Electrodeposited Cu as a Potential Electrode for Electrochemical Reduction Reactions of CO2. *Applied Sciences* **11**, (2021).

27. Cai, Y. *et al.* Insights on forming N,O-coordinated Cu single-atom catalysts for electrochemical reduction CO2 to methane. *Nat Commun* **12**, 586 (2021).

28. Wei, S. *et al.* Construction of single-atom copper sites with low coordination number for efficient CO2 electroreduction to CH4. *J Mater Chem A Mater* **10**, 6187–6192 (2022).

29. Zhao, K. *et al.* Selective electroreduction of CO2 to acetone by single copper atoms anchored on N-doped porous carbon. *Nat Commun* **11**, 2455 (2020).

30. Karapinar, D. *et al.* Electroreduction of CO2 on Single-Site Copper-Nitrogen-Doped Carbon Material: Selective Formation of Ethanol and Reversible Restructuration of the Metal Sites. *Angewandte Chemie International Edition* **58**, 15098–15103 (2019).

31. Yang, H. *et al.* Scalable Production of Efficient Single-Atom Copper Decorated Carbon Membranes for CO2 Electroreduction to Methanol. *J Am Chem Soc* **141**, 12717–12723 (2019).

32. Kim, D., Kley, C. S., Li, Y. & Yang, P. Copper nanoparticle ensembles for selective electroreduction of CO $_2$ to C $_2$ –C $_3$ products. *Proceedings of the National Academy of Sciences* **114**, 10560–10565 (2017).

33. Mistry, H. *et al.* Highly selective plasma-activated copper catalysts for carbon dioxide reduction to ethylene. *Nat Commun* **7**, 12123 (2016).

34. Kim, J. *et al.* Branched Copper Oxide Nanoparticles Induce Highly Selective Ethylene Production by Electrochemical Carbon Dioxide Reduction. *J Am Chem Soc* **141**, 6986–6994 (2019).

35. Kim, D., Kley, C. S., Li, Y. & Yang, P. Copper nanoparticle ensembles for selective electroreduction of CO2 to C2–C3 products. *Proceedings of the National Academy of Sciences* **114**, 10560–10565 (2017).

36. Mistry, H. *et al.* Highly selective plasma-activated copper catalysts for carbon dioxide reduction to ethylene. *Nat Commun* **7**, 12123 (2016).

37. Kohlrausch, E. C. *et al.* A high-throughput, solvent free method for dispersing metal atoms directly onto supports. *J Mater Chem A Mater* **9**, 26676–26679 (2021).

38. Aygün, M. *et al.* Palladium Nanoparticles Hardwired in Carbon Nanoreactors Enable Continually Increasing Electrocatalytic Activity During the Hydrogen Evolution Reaction. *ChemSusChem* **14**, 4973–4984 (2021).

39. del Carmen Gimenez-Lopez, M., Kurtoglu, A., Walsh, D. A. & Khlobystov, A. N. Extremely Stable Platinum-Amorphous Carbon Electrocatalyst within Hollow Graphitized Carbon Nanofibers for the Oxygen Reduction Reaction. *Advanced Materials* **28**, 9103–9108 (2016).

40. Agasti, N. *et al.* Cerium Oxide Nanoparticles Inside Carbon Nanoreactors for Selective Allylic Oxidation of Cyclohexene. *Nano Lett* **20**, 1161–1171 (2020).

41. Popov, I. *et al.* Chemical Kinetics of Metal Single Atom and Nanocluster Formation on Surfaces: An Example of Pt on Hexagonal Boron Nitride. *Nano Lett* **23**, 8006–8012 (2023).

42. Dunwell, M., Luc, W., Yan, Y., Jiao, F. & Xu, B. Understanding Surface-Mediated Electrochemical Reactions: CO2 Reduction and Beyond. *ACS Catal* **8**, 8121–8129 (2018).

43. Reske, R., Mistry, H., Behafarid, F., Roldan Cuenya, B. & Strasser, P. Particle Size Effects in the Catalytic Electroreduction of CO2 on Cu Nanoparticles. *J Am Chem Soc* **136**, 6978–6986 (2014).

44. Gupta, K., Bersani, M. & Darr, J. A. Highly efficient electro-reduction of CO2 to formic acid by nano-copper. *J Mater Chem A Mater* **4**, 13786–13794 (2016).

45. Huang, Y., Deng, Y., Handoko, A. D., Goh, G. K. L. & Yeo, B. S. Rational Design of Sulfur-Doped Copper Catalysts for the Selective Electroreduction of Carbon Dioxide to Formate. *ChemSusChem* **11**, 320–326 (2018).

46. Shinagawa, T., Larrazábal, G. O., Martín, A. J., Krumeich, F. & Pérez-Ramírez, J. Sulfur-Modified Copper Catalysts for the Electrochemical Reduction of Carbon Dioxide to Formate. *ACS Catal* **8**, 837–844 (2018).

47. FRESE, K. W. Chapter 6 - ELECTROCHEMICAL REDUCTION OF CO2 AT SOLID ELECTRODES. in *Electrochemical and Electrocatalytic Reactions of Carbon Dioxide* (ed. Sullivan, B. P.) 145–216 (Elsevier, Amsterdam, 1993). doi:https://doi.org/10.1016/B978-0-444-88316-2.50010-3.

48. C. D. Wagner. Handbook_of_X_ray_Photoelectron_Spectros.

49. Liu, C. *et al.* Stability and Effects of Subsurface Oxygen in Oxide-Derived Cu Catalyst for CO2 Reduction. *The Journal of Physical Chemistry C* **121**, 25010–25017 (2017).

50. Kim, D. *et al.* Insights into an autonomously formed oxygen-evacuated Cu2O electrode for the selective production of C2H4 from CO2. *Physical Chemistry Chemical Physics* **17**, 824–830 (2015).

51. Xiang, H. *et al.* Copper–Indium Binary Catalyst on a Gas Diffusion Electrode for High-Performance CO2 Electrochemical Reduction with Record CO Production Efficiency. *ACS Appl Mater Interfaces* **12**, 601–608 (2020).

52. Hori, Y. Electrochemical CO2 Reduction on Metal Electrodes. in *Modern Aspects of Electrochemistry* (eds. Vayenas, C. G., White, R. E. & Gamboa-Aldeco, M. E.) 89–189 (Springer New York, New York, NY, 2008). doi:10.1007/978-0-387-49489-0_3.

53. Hu, S.-N. *et al.* Sulfur-modified copper synergy with nitrogen-defect sites for the electroreduction of CO2 to formate at low overpotentials. *Electrochim Acta* **422**, 140557 (2022).

54. Hori, Y., Takahashi, I., Koga, O. & Hoshi, N. Selective Formation of C2 Compounds from Electrochemical Reduction of CO2 at a Series of Copper Single Crystal Electrodes. *J Phys Chem B* **106**, 15–17 (2002).

55. Hahn, C. *et al.* Engineering Cu surfaces for the electrocatalytic conversion of CO2: Controlling selectivity toward oxygenates and hydrocarbons. *Proceedings of the National Academy of Sciences* **114**, 5918–5923 (2017).

56. Kortlever, R., Shen, J., Schouten, K. J. P., Calle-Vallejo, F. & Koper, M. T. M. Catalysts and Reaction Pathways for the Electrochemical Reduction of Carbon Dioxide. *J Phys Chem Lett* **6**, 4073–4082 (2015).

57. Feaster, J. T. *et al.* Understanding Selectivity for the Electrochemical Reduction of Carbon Dioxide to Formic Acid and Carbon Monoxide on Metal Electrodes. *ACS Catal* **7**, 4822–4827 (2017).

58. Chatterjee, T., Boutin, E. & Robert, M. Manifesto for the routine use of NMR for the liquid product analysis of aqueous CO2 reduction: from comprehensive chemical shift data to formaldehyde quantification in water. *Dalton Transactions* **49**, 4257–4265 (2020).

59. Han, N. *et al.* Supported Cobalt Polyphthalocyanine for High-Performance Electrocatalytic CO2 Reduction. *Chem* **3**, 652–664 (2017).

60. Anantharaj, S. & Kundu, S. Do the Evaluation Parameters Reflect Intrinsic Activity of Electrocatalysts in Electrochemical Water Splitting? *ACS Energy Lett* **4**, 1260–1264 (2019).

61. Kresse, G. & Joubert, D. From ultrasoft pseudopotentials to the projector augmented-wave method. *Phys Rev B* **59**, 1758–1775 (1999).

62. Kresse, G. & Furthmüller, J. Efficient iterative schemes for ab initio total-energy calculations using a plane-wave basis set. *Phys Rev B* **54**, 11169–11186 (1996).

63. Perdew, J. P., Burke, K. & Ernzerhof, M. Generalized Gradient Approximation Made Simple. *Phys Rev Lett* **77**, 3865–3868 (1996).

64. Grimme, S., Antony, J., Ehrlich, S. & Krieg, H. A consistent and accurate ab initio parametrization of density functional dispersion correction (DFT-D) for the 94 elements H-Pu. *J Chem Phys* **132**, 154104 (2010).

65. Zhao, Q., Martirez, J. M. P. & Carter, E. A. Revisiting Understanding of Electrochemical CO2 Reduction on Cu(111): Competing Proton-Coupled Electron Transfer Reaction Mechanisms Revealed by Embedded Correlated Wavefunction Theory. *J Am Chem Soc* **143**, 6152–6164 (2021).

Supplementary Files

This is a list of supplementary files associated with this preprint. Click to download.

- SupportinginformationUoN.docx